

Drop-on-demand sample delivery for studying biocatalysts in action at X-ray free-electron lasers

Franklin D Fuller^{1,20}, Sheraz Gul^{1,20}, Ruchira Chatterjee¹, E Sethe Burgie², Iris D Young¹, Hugo Lebrette³, Vivek Srinivas³, Aaron S Brewster¹, Tara Michels-Clark¹, Jonathan A Clinger⁴, Babak Andi⁵, Mohamed Ibrahim⁶, Ernest Pastor¹, Casper de Lichtenberg⁷, Rana Hussein⁶, Christopher J Pollock⁸, Miao Zhang⁶, Claudiu A Stan⁹, Thomas Kroll¹⁰, Thomas Fransson⁹, Clemens Weninger^{9,11}, Markus Kubin¹², Pierre Aller¹³, Louise Lassalle¹, Philipp Bräuer^{13,14}, Mitchell D Miller⁴, Muhamed Amin^{1,19}, Sergey Koroidov^{7,9}, Christian G Roessler^{5,19}, Marc Allaire¹, Raymond G Sierra¹¹, Peter T Docker¹³, James M Glowina¹¹, Silke Nelson¹¹, Jason E Koglin¹¹, Diling Zhu¹¹, Matthieu Chollet¹¹, Sanghoon Song¹¹, Henrik Lemke^{11,19}, Mengning Liang¹¹, Dimosthenis Sokaras¹⁰, Roberto Alonso-Mori¹¹, Athina Zouni⁶, Johannes Messinger^{7,15}, Uwe Bergmann⁹, Amie K Boal^{8,16}, J Martin Bollinger Jr^{8,16}, Carsten Krebs^{8,16}, Martin Högbom^{3,17}, George N Phillips Jr^{4,18}, Richard D Vierstra², Nicholas K Sauter¹, Allen M Orville¹³, Jan Kern^{1,11}, Vittal K Yachandra¹ & Junko Yano¹

X-ray crystallography at X-ray free-electron laser sources is a powerful method for studying macromolecules at biologically relevant temperatures. Moreover, when combined with complementary techniques like X-ray emission spectroscopy, both global structures and chemical properties of metalloenzymes can be obtained concurrently, providing insights into the interplay between the protein structure and dynamics and the chemistry at an active site. The implementation of such a multimodal approach can be compromised by conflicting requirements to optimize each individual method. In particular, the method used for sample delivery greatly affects the data quality. We present here a robust way of delivering controlled sample amounts on demand using acoustic droplet ejection coupled with a conveyor belt drive that is optimized for crystallography and spectroscopy measurements of photochemical and chemical reactions over a wide range of time scales. Studies with photosystem II, the phytochrome photoreceptor, and ribonucleotide reductase R2 illustrate the power and versatility of this method.

X-ray scattering, X-ray crystal diffraction (XRD) and X-ray spectroscopy are valuable tools for studying biomolecular mechanisms

because they yield direct and element-specific molecular geometry and electronic-state information. X-ray signals generated by excitation with <50-fs pulses from an X-ray free-electron laser (XFEL) are produced before radiation-induced changes occur (picosecond time scale)^{1–4}. Consequently, XFELs provide new opportunities to study biomolecules at ambient temperature and to probe enzymatic reaction intermediates prepared *in situ*. To understand enzymatic mechanisms in detail, both electronic and molecular structural information are needed for the reaction intermediates, and in practice this requires that complementary time-resolved methods be used to probe the reaction. Time-resolved studies of biomolecules, however, are challenging with an XFEL, because the focused XFEL pulses destroy the sample after each shot. This requires that the sample be continually replenished in a consistent state, with temporal delays from reaction initiation to the X-ray probe in the picosecond to seconds time scale^{5,6}.

Recently, we reported an approach for simultaneously collecting XRD data and X-ray emission spectroscopy (XES) data, with the goal of investigating catalysis in metalloenzymes⁴. XES directly probes the redox and spin state of the active site metal(s) and

¹Molecular Biophysics and Integrated Bioimaging Division, Lawrence Berkeley National Laboratory, Berkeley, California, USA. ²Department of Biology, Washington University in St. Louis, St. Louis, Missouri, USA. ³Department of Biochemistry and Biophysics, Stockholm University, Stockholm, Sweden. ⁴Department of BioSciences, Rice University, Houston, Texas, USA. ⁵National Synchrotron Light Source II, Brookhaven National Laboratory, Upton, New York, USA. ⁶Institut für Biologie, Humboldt-Universität zu Berlin, Berlin, Germany. ⁷Institutionen för Kemi, Kemiskt Biologiskt Centrum, Umeå Universitet, Umeå, Sweden. ⁸Department of Chemistry, Pennsylvania State University, University Park, Pennsylvania, USA. ⁹Stanford PULSE Institute, SLAC National Accelerator Laboratory, Menlo Park, California, USA. ¹⁰SSRL, SLAC National Accelerator Laboratory, Menlo Park, California, USA. ¹¹LCLS, SLAC National Accelerator Laboratory, Menlo Park, California, USA. ¹²Institute for Methods and Instrumentation on Synchrotron Radiation Research, Helmholtz Zentrum Berlin für Materialien und Energie GmbH, Berlin, Germany. ¹³Diamond Light Source Limited, Harwell Science and Innovation Campus, Didcot, UK. ¹⁴Department of Biochemistry, University of Oxford, Oxford, UK. ¹⁵Department of Chemistry–Ångström, Molecular Biomimetics, Uppsala University, Uppsala, Sweden. ¹⁶Department of Biochemistry and Molecular Biology, Pennsylvania State University, University Park, Pennsylvania, USA. ¹⁷Department of Chemistry, Stanford University, Stanford, California, USA. ¹⁸Department of Chemistry, Rice University, Houston, Texas, USA. ¹⁹Present addresses: Center for Photonics and Smart Materials, Zewail City of Science and Technology, Giza, Egypt (M.A.), Ventana Medical Systems, Inc., Tucson, Arizona, USA (C.G.R.), and SwissFEL, Paul Scherrer Institut, Villigen, Switzerland (H. Lemke). ²⁰These authors contributed equally to this work. Correspondence should be addressed to J.K. (jfkern@lbl.gov), V.K.Y. (vkyachandra@lbl.gov) or J.Y. (jyano@lbl.gov).

ensures that the atomic structure revealed by XRD is in the correct catalytic state. However, optimal sample delivery conditions (crystal size, sample path lengths for spectroscopy, overall sample consumption, etc.) for collecting the XRD and XES data sets are not the same. Several continuous-flow sample delivery strategies for XFEL experiments have been established (Fig. 1a)^{7–10}. Liquid jet systems, such as the gas dynamic virtual nozzle (GDVN)⁷ and the microfluidic electrokinetic sample holder (MESH)⁸, use small crystals to obtain the flow rates reported (as a consequence of the narrow feed capillaries they use), whereas lipidic cubic phase (LCP) or grease matrix injectors^{9,10} use a highly viscous medium to achieve low flow rates with medium-sized capillaries. Acoustic droplet ejection (ADE) has a high upper bound for the crystal size while keeping sample consumption at low levels, which is orders of magnitude lower than Rayleigh jets of the same path length. Fixed-target systems have also been successfully used at XFEL facilities^{11–14}, but such systems have not yet been demonstrated for multimodal data collection.

ADE offers a sweet spot in sample consumption rate and available path length to accommodate simultaneous XES and XRD analysis of biomolecules^{15,16}. To extend the ADE method to probe longer temporal delays (milliseconds to a few seconds) after the initiation of reactions and/or more complex reaction-initiation schemes, we describe here a conveyor belt system. The conveyor belt continuously transports droplets containing crystal slurry or protein solution through the reaction region, which consists of either an array of laser excitations for photochemical reactions or a gas-activation area for chemically triggered reactions (Fig. 1b,c and Supplementary Fig. 1). The sample delivery parameters used here were optimized for crystals with a diameter of 20–100 μm , solvent path lengths of 200–300 μm and sample consumption volumes of 0.8–6.0 nl/shot, with sample replacement rates of up to 120 Hz.

To demonstrate that this drop-on-tape (DOT) method is versatile for capturing reaction intermediates, we show here two types of reactions that are triggered and observed *in situ* by $\text{K}\beta_{1,3}$ or $\text{K}\alpha$ XES using solution samples: (i) the water oxidation reaction of photosystem II (PS II), which requires multiple timed laser excitations, and (ii) an O_2 -activation reaction at the Mn(II)–Fe(II) cluster of the class Ic ribonucleotide reductase R2 (RNR) from *Chlamydia trachomatis* (Ct), which yields the active Mn(IV)–Fe(III) cluster via a Mn(IV)–Fe(IV) intermediate^{17–19}. The application of a DOT approach to crystallography is further demonstrated by atomic-resolution XRD data of a bilin-containing phytochrome photoreceptor and the simultaneous XRD and XES analysis of the Mn–Fe RNR.

RESULTS

The drop-on-tape setup

The conveyor belt is the core component of our DOT sample-delivery technique, and it was used to build a queue of droplets (Fig. 1b, top right) that arrive at the XFEL beam in a desired state of preparation. Droplets were deposited, synchronous with the XFEL pulse arrival, from an open 2.5-mm diameter reservoir onto a polyimide belt using ADE¹⁵. ADE can eject large crystals without complications such as orifice clogging, which commonly plagues delivery systems using narrow (<100 μm) capillaries. A wide (~250 μm) capillary supply line maintains constant reservoir levels (Fig. 1b, top left), allowing ejection conditions to

remain stable and maintenance free for hours. A focused XFEL beam (<25 μm^2) that passes parallel to the belt surface probes the droplet on the belt. After X-rays probe the sample, the belt is cleaned before it loops back to the starting point.

DOT is well suited for probing a wide range of photochemical reactions in enzymes and inorganic systems. Excitation periods that range from seconds to hundreds of milliseconds are accessible by positioning an evenly spaced array of laser-excitation points along the belt (Fig. 2a). Shorter delays (femtoseconds to hundreds of milliseconds) are accessed by a movable excitation point near the X-ray interaction region (Fig. 1b). The length of the time delay is the ratio of the distance (D) between the points of reaction initiation and X-ray interaction to the tangential velocity of the belt (v). The precision of the belt velocity required to achieve a desired time delay is determined by the ratio of the droplet diameter to the delay, where longer delay times and smaller droplets require higher precision. Delays of at least 3 s were readily achieved with 270- μm droplets (Fig. 2a). In liquid jet systems, by contrast, excitation pulses for delay times longer than 10 ms need to be coupled into the capillary that supplies the jet, as was implemented for previous PS II studies²⁰. The current method, with discrete excitation in a droplet-based system, is more flexible for multistep excitation experiments and prevents population mixing that can result from laminar flow in a capillary.

Photoactivation of photosystem II

Figure 2a shows the DOT setup that was used to study PS II catalytic intermediates in solution. The setup was also used in recently reported studies of PS II crystal samples²¹. The oxidation of water by PS II requires multiple laser flashes to complete the four-electron redox chemistry that is catalyzed by the Mn_4CaO_5 cluster^{22,23}. This complex reaction progresses through four intermediates, called S states (Fig. 2b). Long delay times between flashes (0.1–1.0 s) are required to ensure nearly complete production of each successive S state due to a slow, rate-limiting movement of quinone^{24,25}. To accommodate this intricate reaction mechanism, we implemented a feedback control system of the belt speed and deposition delay, which affected the flashing period and droplet phase, respectively. This was provided by a pair of optical gates that reported the arrival time of the droplet stream in the excitation grid (Fig. 2a and Supplementary Fig. 1).

$\text{K}\beta_{1,3}$ emission (metal 3p to 1s transition) is sensitive to oxidation and spin state^{26,27} and serves as an indicator of the S-state advancement in PS II (ref. 28). Figure 2c shows the Mn $\text{K}\beta_{1,3}$ XES difference spectra of PS II in solution that was collected with the DOT method. Droplets (270 μm diameter; ~5 nl) were injected onto the conveyor belt at room temperature in a helium atmosphere (Fig. 1b). The emission signal was collected with a 16-crystal wavelength-dispersive von Hamos spectrometer^{29,30}, which collects the full $\text{K}\beta_{1,3}$ energy range³¹ without scanning. These data are in good agreement with those collected at a synchrotron source using the freeze-quench method for preparing PS II solution in different S states²⁶ (Fig. 2c). On one hand, in the transition from the dark S_1 state (0F; F: flash) to the most oxidized 2F (S_3 -rich) state, a negative difference on the high-energy side of the peak was seen, indicating oxidation. On the other hand, a clear positive difference relative to 2F at the high-energy side was seen after illumination to the 3F (S_0 -rich) state, indicating transition of the major fraction of PS II from the S_3 state to the most reduced S_0

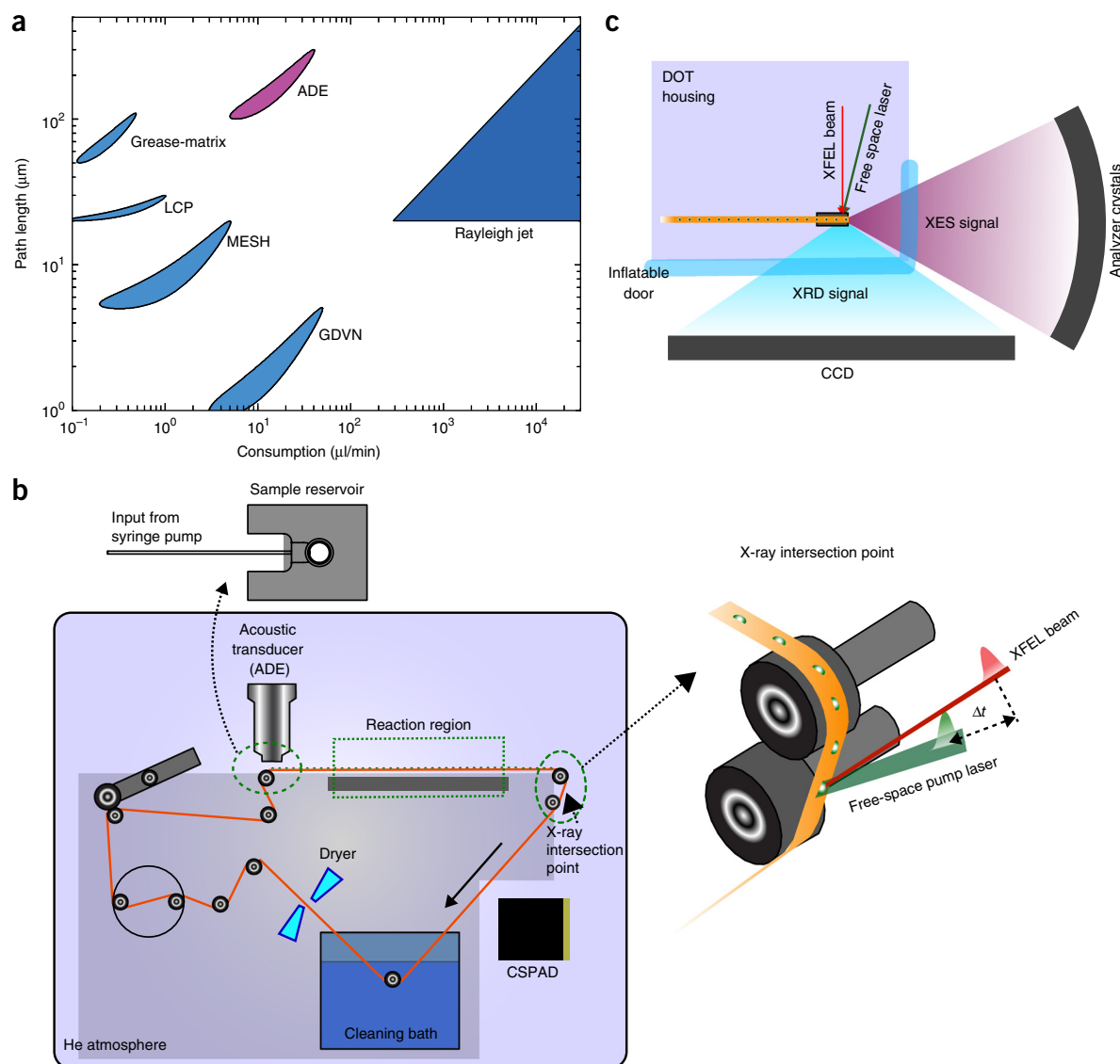


Figure 1 | Experimental setup. (a) Qualitative comparison of sample-consumption rate (assuming 120 Hz operation) and path length accessible with the replenishing methods used at XFELs. (b) Schematic for DOT setup for experiments. The conveyor belt delivers droplets of sample at a high rate (up to 120 Hz). A large (283-liter) gas-tight chamber houses the entire instrument and is maintained at 95–97% helium via a 30 ft³/h purge flow. Droplets are deposited onto a polyimide belt by ADE from an open 2.5-mm-in-diameter reservoir that is continuously resupplied via a capillary feed line attached to a syringe pump (top left). In the interaction region, the belt is run at a small angle with respect to the z-axis (vertical) in the x,z plane (right; zoomed-in view of interaction point). Positioning the droplet in the X-ray focus is accomplished by moving the entire system in the horizontal plane, while the droplet z-position (vertical) on the tape at the intersection is adjusted by changing the deposition delay. The belt is cleaned and dried *in situ*, enabling continuous use for days. The reaction initiation point for longer time delays is shown in the green box. The XFEL beam passes parallel to the belt surface, striking the droplet, which is on the belt (right). (c) Schematic for the data collection geometry for XRD and XES. An inflatable (and X-ray transparent) plastic film door with a 160° aperture to the X-ray interaction region allows both XES and XRD to be collected simultaneously.

state. Comparable difference amplitudes between spectra obtained from a freeze–quench method and spectra obtained using the DOT method at room temperature indicate that the purity of the S-state populations from both methods are similar.

Chemical activation of ribonucleotide reductase by gas exposure

The DOT setup can also be used to study chemically activated reactions. To demonstrate this, we examined O₂ activation of a solution of the Ct RNR protein by replacing the laser excitation grid with an incubation chamber that exposes the drops to

O₂ gas as they travel to the X-ray beam (Fig. 3a,b). We built a chamber that exposed a 60-mm portion of the conveyor belt to a 4.7 liter/min O₂ flow. Leakage of O₂ to the surrounding helium environment was mitigated by using a flow-through exhaust design, guard baffles and differential pumping. Tape speed through the chamber determines the gas exposure time, and we explored a range of exposures from 0.5 to 8 s.

Figure 3c shows the Fe K α_1 and K α_2 XES difference spectra of the Fe–Mn RNR solution in which we monitored the advancement of the Fe site from its reduced form, Fe(II), to the oxidized form by varying O₂ exposure time. Both K α_1 and K α_2 exhibit spectral

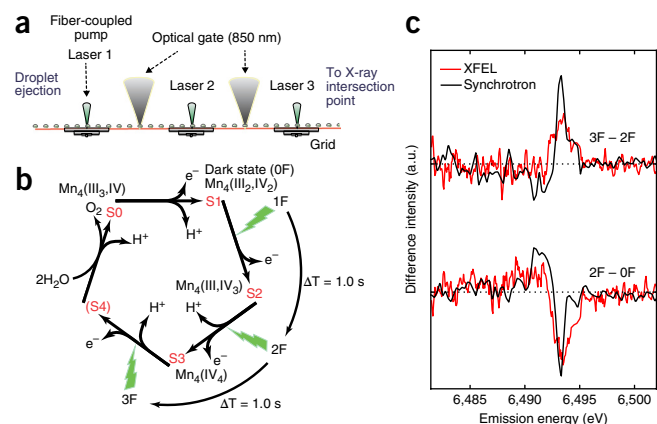


Figure 2 | Photo-initiated XES of PS II. (a) The photoexcitation setup used for PS II, which is comprised of a precision-machined grid of fixed excitation positions with 60-mm spacing. Optical gates, which measure droplet arrival times on the grid, are realized by two low-power (<0.5 mW) continuous-wave near-infrared (NIR, 850 nm) point sources, delivered via optical fiber. NIR light scatters from the droplets as they pass over the gates and is collected onto high-speed silicon photodiodes for readout. (b) Schematic of the mechanism depicting S-state advancement using periodic laser flashes. The interval between laser flashes (ΔT) for both DOT and freeze-quench methods was 1.0 s. Flash states (denoted as 0F, 1F, 2F or 3F) are highly enriched in the pure reaction intermediates S_1 , S_2 , S_3 and S_0 , respectively, but are not completely pure due to small back-reaction rates and photon misses²³. (c) A comparison of Mn $K\beta_{1,3}$ XES difference spectra of PS II solution collected with the DOT instrument at room temperature using an XFEL (red) and the same state differences collected by using a freeze-quench method at a temperature of 8 K with a synchrotron source (black). The XFEL spectra contain about 120,000 shots per difference spectrum. a.u., arbitrary units. For details of the collection conditions and difference analysis, see Online Methods and **Supplementary Figure 7**.

changes as a function of O_2 -exposure time. The full-width half-maximal (FWHM) value of the $K\alpha_1$ line, which serves as a proxy for oxidation state^{32,33}, showed the reaction progressing toward peak oxidation at 2 s and then reduction again at 8 s exposure, which roughly matched the expected changes for the formation of a Mn(IV)–Fe(IV) intermediate and subsequent decay to a Mn(IV)–Fe(III) form (**Fig. 3b**)^{17–19}. The difference spectra with respect to the 8 s O_2 exposure show that the Fe $K\alpha$ spectra contain complex line-shape changes, with both shifts and width changes throughout the reaction cycle. We note that no significant signs of droplet dehydration were detected for these studies of RNR solution. In samples containing a substantial amount of polyethylene glycol (PEG), as in many protein crystal buffers, PEG diffraction appeared if the belt droplets were exposed to helium for too long. The lower bound belt speed is thus limited by sample dehydration and needs to be evaluated on a per-sample basis.

For X-ray spectroscopy studies, as described above, the ability to control path lengths (for example, $1/e$ is 520 μm at 6,500 eV for water) is important for efficient data collection, by balancing the sample-consumption rate and the data-acquisition time. The acoustic pulse in the ADE system can be tuned to provide a range of droplet sizes (50–400 μm in diameter), with larger droplets simply requiring a lower central frequency and/or higher driving force. The ability to access larger droplets is particularly beneficial for collecting signals from weaker transitions, such as $K\beta_{2,5}/K\beta''$, that can uniquely probe changes in the metal–ligand environment while its intensity is ~ 60 times lower than that of $K\beta_{1,3}$ (ref. 27).

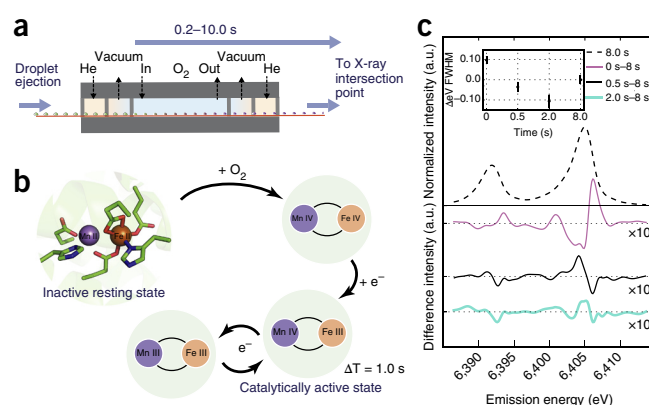


Figure 3 | XES of gas-activated RNR. (a) Schematic of the differentially pumped O_2 gas activation setup containing regions of O_2 gas and slight negative pressure (vacuum). (b) The known reaction scheme of Ct RNR^{17–19} is shown. O_2 is activated at the Mn(II)–Fe(II) cluster to produce a high-valent Mn(IV)–Fe(IV) intermediate in a biomolecular reaction ($k_{\text{form}} = 13 \pm 3 \text{ mM}^{-1}\text{s}^{-1}$ at 5 °C from the literature¹⁸), which then decays to the active Mn(IV)–Fe(III) state (first-order $k_{\text{decay}} = 0.02 \text{ s}^{-1}$ at 5 °C also from the literature¹⁸). (c) RNR solution was monitored at 25 °C with Fe $K\alpha$ emission for various O_2 exposure times. The inset shows the $K\alpha_1$ FWHM as a function of exposure time relative to an 8 s exposure. Error bars were computed via bootstrap residual sampling (1,000 samples per data point). Difference spectra with respect to an 8 s exposure (smoothed by wavelet denoising and 10 \times magnification) are shown in the main plot.

Femtosecond crystallography using the DOT setup

ADE's ability to adjust droplet size also allows for a wide range of crystal sizes to be analyzed, whereas the discrete nature of delivery keeps sample consumption at moderate levels. Crystals >20 μm in size are of general interest for serial femtosecond crystallography (SFX)^{2–4}, as their larger crystal volume, in comparison to <5 μm crystals used in many liquid jet systems, can translate to stronger diffraction signals and potentially higher resolution. Also, diffraction quality may be more easily optimized at synchrotron beam lines before XFEL experiments for crystals in this size range. For the XRD results presented here, we used 5.5 nl droplets (~ 270 to 290 μm hemispheres) with crystal sizes that ranged from 20 to 100 μm . With this droplet size, a 100% droplet hit rate was achieved with favorable signal collection rates and reasonable sample consumption (3.3 $\mu\text{l}/\text{min}$ at 10 Hz). XRD solvent background was present, but manageable with a beam focus of $\sim 5 \mu\text{m}$. Thus, the solvent path length that can be achieved with the DOT setup (100–300 μm) is practical, as seen in the Results section, for the study of the crystals surveyed here. However, practical considerations of what droplet size to select for which crystal size must be made for balancing the diffractivity of crystals and the solvent background; there is a pragmatic trade-off between factors favoring smaller droplets (such as solvent background and sample consumption) and those favoring larger droplets (such as instrument precision and distance of the X-ray beam from the belt). A consideration for XRD, which is unique to this setup, is polymer scatter and absorption from the polyimide conveyor belt. Polymer scatter was typically lower in amplitude than solvent scatter, and absorption was successfully treated in the post analysis (**Supplementary Fig. 2**).

To explore the applicability of the DOT setup for different protein crystals, we examined four samples: two different phytochrome constructs (50 μm plates or 100 μm needles), RNR

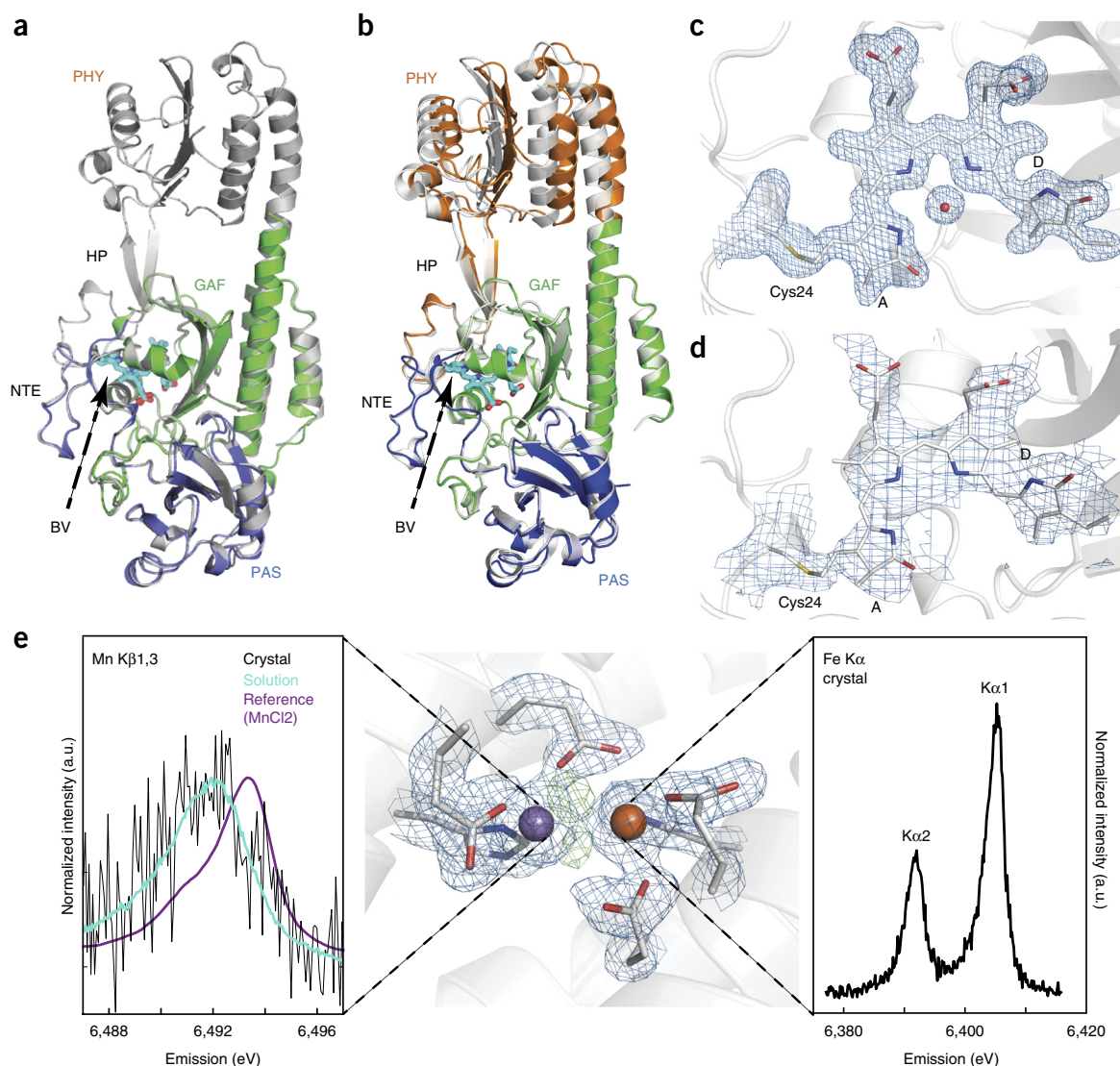


Figure 4 | XRD of various enzymes. (a) Structures of the PAS-GAF (blue and green, respectively) and PSM (white) domains from *D. radiodurans* BphP in their dark-adapted Pr states are shown superimposed. HP, hairpin; NTE, amino-terminal extension; BV, biliverdin. (b) Superposition of atomic models of the PSM in the room-temperature Pr state (colored) with that derived from diffraction data collected at a temperature of 100 K (white; PDB ID 4Q0J). The β -sheets of the GAF domains were superimposed, allowing the respective positions of the PAS and PHY domains of the two models to be identified. The largest differences between the models were found at the PHY domain. For the model derived from the data collected at room temperature, the domains were colored blue, green and orange for the PAS, GAF and PHY domains, respectively. BV from the room temperature structure is shown for orientation. (c,d) Composite simulated annealing omit maps ($2F_o - F_c$) contoured at 1σ were superimposed with the corresponding PAS-GAF (c) or PSM (d) model of DrBphP²². For clarity, only the electron density around Cys24 (gray; c,d), biliverdin (cyan; c,d) and the pyrrole water (c, red sphere) is shown. Labels A and D indicate the first and fourth pyrrole rings of the BV chromophore, respectively. (e) Metal-site electron density ($2F_o - F_c$) at the heterodinuclear Mn-Fe site in an aerobic class Ic RNR, metal ions and protein ligands are shown (contoured to 1.3σ) in blue. Residual positive-difference electron density ($F_o - F_c$), which represents non-protein ligands, is shown in green (contoured to 3.5σ). The Mn and Fe atoms are depicted as purple and orange spheres, respectively. $K\beta_{1,3}$ XES of oxidized RNR in crystal and in solution collected at room temperature with an XFEL is shown to the left. A Mn(II)Cl₂ calibration standard is also shown to illustrate the absolute oxidation state of the solution and crystal spectra. Fe K α XES data collected from oxidized RNR crystals is shown at the right.

(20- to 30- μ m bipyramidal crystals) and PS II (20- to 50- μ m bipyramidal crystals) (Supplementary Fig. 3 and Supplementary Table 1). To collect diffraction data from crystals of various sizes without saturating the detector, we used a high-dynamic-range Rayonix MX 170 HS detector, operated at its maximum data rate of 10 Hz in the 2×2 binning mode. For all of the crystallography data presented here, an incident X-ray energy of 9.5–9.8 keV was used. High-resolution structures derived from experiments done at room temperature were obtained in all cases

(Supplementary Table 2)²¹. Data collection times varied depending on the crystal number density, but complete data sets could be collected in ~40–80 min with 10% to 50% of all shots giving indexed diffraction patterns (Supplementary Fig. 4 and Supplementary Table 1).

Room temperature structures of phytochromes

XRD data were collected for the chromophore-binding region of the bacterial phytochrome (BphP) from *Deinococcus radiodurans*,

which contains only the Per–Arnt–Sim (PAS) and cGMP phosphodiesterase–adenylyl cyclase–FhlA (GAF) domains (residues 1–321), or the entire photosensory module (PSM; residues 1–501) in their dark-adapted (Pr) states (**Supplementary Table 2**). These data yielded previously unknown room-temperature-derived structures of DrBphP dimers at 1.65-Å and 3.3-Å resolution, respectively (**Fig. 4a,b**). The chromophore-binding pocket of the PAS–GAF biliprotein was highly congruent with the best resolved structure of the DrBphP PSM domain (DrBphP-PSM) to date³⁴, but it diverged from an alternate binding-pocket orientation seen for recently reported monomeric crystal assemblies of DrBphP^{35,36} and the photochemically compromised Asp207Ala mutant (**Supplementary Fig. 5**)³⁴. Whether both bilin configurations represent authentic structural microstates of the Pr photo-state in BphP dimers is not yet known. Additionally, we detected a marked shift of the phytochrome-specific domain (PHY) within the crystal lattice of the PSM dimer, as compared to the models generated with diffraction data collected at 100 K, suggesting that cryopreservation and/or cryogenic temperatures perturb the structure and/or dynamics of the GAF and PHY domains (**Fig. 4b**).

Phytochromes undergo a cascade of conformational changes after photoexcitation of the bilin chromophore, with dynamics that span from picoseconds to milliseconds^{37–39}. However, the electronic state of the bilin chromophore is exceedingly sensitive to radiation-induced changes from synchrotron X-ray sources⁴⁰, which culminate in rupture of the thioether linkage between the Cys24 and the bilin moiety at high dose. These complications were eliminated in our XFEL data (**Fig. 4c,d**), with both structures clearly showing continuous electron density along the thioether–bilin linkage, which were already visible in the initial $F_o - F_c$ omit maps (**Supplementary Fig. 6**). The ability to collect room-temperature-derived structures of phytochrome that are free of radiation-induced artifacts thus opens the possibility of elucidating bona fide structures of phytochrome photoconversion intermediates.

Combined X-ray emission and crystallography of ribonucleotide reductase

We also collected a high-resolution room-temperature-derived structure of the *Saccharopolyspora erythraea* Mn–Fe RNR (**Fig. 4e**). Ribonucleotide reductases are the only enzymes that catalyze the reduction of ribonucleoside-5'-diphosphates or ribonucleoside-5'-triphosphates (NDPs or NTPs) to the 2'-deoxynucleotides (dNDPs or dNTPs). Class I RNRs generate an essential catalytic radical via a dinuclear metal site, involving redox-state changes at the metal site⁴¹. XES can be collected simultaneously with XRD for many metalloproteins, serving as a sensitive *in situ* verification of state preparation. To demonstrate this, we collected a Mn $K\beta_{1,3}$ and Fe $K\alpha$ spectrum of Mn–Fe RNR, simultaneous with XRD, from crystal slurries (**Fig. 4e**). Mn XES data from RNR protein crystals was overlaid with a solution spectrum, using the same dispersive X-ray emission spectrometer system. The results confirmed that the XRD data collected, and thus the electron density obtained, represent the metal site in its as-prepared oxidized form and that the Mn ion was not photo-reduced to the Mn(II) state before probing the scattering data. Model building and refinement is currently underway and will be reported elsewhere.

DISCUSSION

Through the XRD and XES results reported here, we demonstrate that the DOT sample delivery method provides a foundation for multimodal data collection in both solution and crystalline samples. The conveyor belt in the DOT setup is flexible and extensible, and it permits either photochemical or chemical activation of samples *in situ*, thus enabling its use to study a wide variety of transient reaction intermediates. For photochemical reactions, in particular, the ability to precisely illuminate a discrete volume eliminates potential flow-induced state-mixing before probing the sample. Here we carried out the gas-activation studies of a solution sample, but the method can also be applied to crystalline samples; the influence of substrate transport speed on the observed kinetics would depend on crystal size.

Another extension of the current work that we envision is liquid mixing before probing the droplet. This would enable a much broader class of enzyme–substrate studies. For reactions with relatively slow kinetics (seconds time scale) where liquids can be mixed right before droplet ejection, the method as it is shown can already be applied. Faster reactions can be probed by incorporating a rapid mixing scheme directly either in droplet creation or shortly after deposition on to the belt.

METHODS

Methods, including statements of data availability and any associated accession codes and references, are available in the [online version of the paper](#).

Note: Any Supplementary Information and Source Data files are available in the online version of the paper.

ACKNOWLEDGMENTS

We thank T. Rendahl from LCLS for help with controls and B. Martins, S. Myers, M. Cowan, G. Shea-McCarthy and C. Whalen (Brookhaven National Laboratory) for help with engineering and controls, R. Ellson, J. Olechno, R. Stearns and B. Hadimioglu (LBNL) for sharing their experience with the acoustic transducers and related issues, C. Saracini (LBNL) for his help with the preliminary testing of the DOT system, P. Glatzel (ESRF) for discussion of the Fe $K\alpha$ emission and F. Houle (LBNL) for sharing her reaction–diffusion simulation software Kinetoscope and for useful discussions. This work was supported by the Director, Office of Science, Office of Basic Energy Sciences (OBES), Division of Chemical Sciences, Geosciences and Biosciences (CSGB) of the US Department of Energy (DOE) under contract DE-AC02-05CH11231 (J.Y. and V.K.Y.) for X-ray methodology and instrumentation, by the US National Institutes of Health (NIH) grants GM110501 (J.Y.) for instrumentation development for XFEL experiments, GM102520 (N.K.S.) and GM117126 (N.K.S.) for development of computational protocols for XFEL data and GM055302 (V.K.Y.) for PS II biochemistry, structure and mechanism, a Ruth L. Kirschstein National Research Service Award (5 F32 GM116423-02; F.D.F.), the Human Frontiers Science Project award no. RGP0063/2013 310 (J.Y., U.B. and A.Z.), and the Science and Technology Center program of the US National Science Foundation (NSF) through BioXFEL under agreement no. 1231306 (J.A.C., M.D.M. and G.N.P.). R.D.V. is supported by NSF grant MCB-1329956. J.A.C. was supported by a training fellowship from the Gulf Coast Consortia on the Houston Area Molecular Biophysics Program (NIHGM grant no. T32GM008280). C.J.P. was supported by NIH NRSA grant GM113389-01. Portions of this work were supported by Brookhaven National Laboratory (BNL)–US DOE, Laboratory Directed Research and Development grant 11-008 (C.G.R., M. Allaire, A.M.O.), NIH–NCRR grant 2-P41-RR012408 (A.M.O. and M. Allaire), NIH–National Institute of General Medical Sciences (NIGMS) grants 8P41GM103473-16 (A.M.O.) and Y1GM008003 (M. Allaire) and US DOE, Office of Biological and Environmental Research (OBER) grant FWP B0-70 (A.M.O. and B.A.). A.M.O., P.A. and P.T.D. were supported in part by Diamond Light Source, and A.M.O. acknowledges support from a Strategic Award from the Wellcome Trust and the Biotechnology and Biological Sciences Research Council (grant 102593). P.B. was supported by a Wellcome Trust DPhil studentship. M.H. received support from the Knut and Alice Wallenberg Foundation, the Swedish Cancer Society, the Wenner–Gren foundations and the Swedish

Research Council (grants 2013-541 and 2013-5884). C.A.S. acknowledges support from the US DOE, Office of Science, Division of CSGB. A.Z. acknowledges support from the DFG-Cluster of Excellence 'UniCat', coordinated by the Technische Universität Berlin, and Sfb1078 (Humboldt Universität Berlin), TP A5. J.M. acknowledges support from the Solar Fuels Strong Research Environment (Umeå University), the Artificial Leaf Project (K&A Wallenberg Foundation 2011.0055) and Energimyndigheten (36648-1). This research work used resources from the National Energy Research Scientific Computing Center, a DOE Office of Science User Facility supported by the Office of Science, DOE, under contract no. DE-AC02-05CH11231. Testing of crystals and various parts of the setup were carried out at synchrotron facilities that were provided by the Advanced Light Source (ALS) in Berkeley and the Stanford Synchrotron Radiation Light Source (SSRL) in Stanford, which were funded by the DOE OBES. The SSRL Structural Molecular Biology Program is supported by the DOE Office of Biological and Environmental Research, and by the NIH (grant P41GM103393). Use of the Linac Coherent Light Source (LCLS) and SSRL, SLAC National Accelerator Laboratory, is supported by the US DOE, Office of Science, OBES under contract no. DE-AC02-76SF00515. BNL's contribution to data collection at the LCLS is supported by the Life Science and Biomedical Technology Research (LSBR) program at the National Synchrotron Light Source II (NSLS-II), which operates under a DOE BER contract (DE-SC0012704) and DOE BES contract (DE-AC02-98CH10886), and is supported by NIH-NIGMS grant P41GM111244.

AUTHOR CONTRIBUTIONS

A.M.O., J.K., V.K.Y. and J.Y. conceived the experiment; F.D.F., S.G., J.K., V.K.Y. and J.Y. designed the experiment; E.S.B., R.C., C.J.P., J.A.C., M.I., R.H., A.Z., H. Lebrete, V.S., M.Z., S.K., J.M., A.K.B., J.M.B., C.K., M.H., G.N.P. and R.D.V. prepared, characterized and provided the phytochrome, PS II and RNR samples; F.D.F., J.K., S.G., C.G.R. and A.M.O. designed the acoustic injectors; F.D.F., S.G., B.A., E.P., C.d.L., C.A.S., C.G.R., R.G.S., T.K., M.K., S.K., P.T.D., U.B., G.N.P., J.K., V.K.Y., A.M.O. and J.Y. performed the SFX and XES experiments; J.M.G., C.A.S., S.N., J.E.K., D.Z., M.C., S.S., H. Lemke, D.S., M.L. and R.A.-M. set up the beam lines; A.S.B., I.D.Y., T.M.-C., P.A., P.B., L.L., M.D.M., T.K., M. Amin, M. Allaire, F.D.F., J.K., E.S.B., T.F., C.W. and N.K.S. performed XRD and XES data analysis; F.D.F., J.K., E.S.B., A.M.O., V.K.Y. and J.Y. wrote the paper with contributions from all authors.

COMPETING FINANCIAL INTERESTS

The authors declare no competing financial interests.

Reprints and permissions information is available online at <http://www.nature.com/reprints/index.html>.

- Emma, P. *et al.* First lasing and operation of an Ångström-wavelength free-electron laser. *Nat. Photonics* **4**, 641–647 (2010).
- Chapman, H.N. *et al.* Femtosecond X-ray protein nanocrystallography. *Nature* **470**, 73–77 (2011).
- Boutet, S. *et al.* High-resolution protein structure determination by serial femtosecond crystallography. *Science* **337**, 362–364 (2012).
- Kern, J. *et al.* Simultaneous femtosecond X-ray spectroscopy and diffraction of photosystem II at room temperature. *Science* **340**, 491–495 (2013).
- Benkovic, S.J. & Hammes-Schiffer, S. A perspective on enzyme catalysis. *Science* **301**, 1196–1202 (2003).
- Levantino, M., Yorke, B.A., Monteiro, D.C., Cammarata, M. & Pearson, A.R. Using synchrotrons and XFELs for time-resolved X-ray crystallography and solution scattering experiments on biomolecules. *Curr. Opin. Struct. Biol.* **35**, 41–48 (2015).
- DePonte, D.P. *et al.* Gas dynamic virtual nozzle for generation of microscopic droplet streams. *J. Phys. D Appl. Phys.* **41**, 195505 (2008).
- Sierra, R.G. *et al.* Nanoflow electrospraying serial femtosecond crystallography. *Acta Crystallogr. D Biol. Crystallogr.* **68**, 1584–1587 (2012).
- Weierstall, U. *et al.* Lipidic cubic-phase injector facilitates membrane protein serial femtosecond crystallography. *Nat. Commun.* **5**, 3309 (2014).
- Sugahara, M. *et al.* Grease matrix as a versatile carrier of proteins for serial crystallography. *Nat. Methods* **12**, 61–63 (2015).
- Hunter, M.S. *et al.* Fixed-target protein serial microcrystallography with an X-ray free-electron laser. *Sci. Rep.* **4**, 6026 (2014).
- Baxter, E.L. *et al.* High-density grids for efficient data collection from multiple crystals. *Acta Crystallogr. D Struct. Biol.* **72**, 2–11 (2016).
- Roedig, P. *et al.* Room-temperature macromolecular crystallography using a micropatterned silicon chip with minimal background scattering. *J. Appl. Crystallogr.* **49**, 968–975 (2016).
- Oghbaei, S. *et al.* Fixed target combined with spectral mapping: approaching 100% hit rates for serial crystallography. *Acta Crystallogr. D Struct. Biol.* **72**, 944–955 (2016).
- Roessler, C.G. *et al.* Acoustic injectors for drop-on-demand serial femtosecond crystallography. *Structure* **24**, 631–640 (2016).
- Roessler, C.G. *et al.* Acoustic methods for high-throughput protein crystal mounting at next-generation macromolecular crystallographic beamlines. *J. Synchrotron Radiat.* **20**, 805–808 (2013).
- Griese, J.J., Srinivas, V. & Högbom, M. Assembly of nonheme Mn–Fe active sites in heterodinuclear metalloproteins. *J. Biol. Inorg. Chem.* **19**, 759–774 (2014).
- Jiang, W., Hoffart, L.M., Krebs, C. & Bollinger, J.M. Jr. A manganese(IV)–iron(IV) intermediate in assembly of the manganese(IV)–iron(III) cofactor of *Chlamydia trachomatis* ribonucleotide reductase. *Biochemistry* **46**, 8709–8716 (2007).
- Jiang, W. *et al.* A manganese(IV)–iron(III) cofactor in *Chlamydia trachomatis* ribonucleotide reductase. *Science* **316**, 1188–1191 (2007).
- Kern, J. *et al.* Taking snapshots of photosynthetic water oxidation using femtosecond X-ray diffraction and spectroscopy. *Nat. Commun.* **5**, 4371 (2014).
- Young, I.D. *et al.* Structure of photosystem II and substrate binding at room temperature. *Nature* **540**, 453–457 (2016).
- Kok, B., Forbush, B. & McGloin, M. Cooperation of charges in photosynthetic O₂ evolution—I. a linear four-step mechanism. *Photochem. Photobiol.* **11**, 457–475 (1970).
- Renger, G. *Primary Processes of Photosynthesis: Principles and Apparatus* (Royal Society of Chemistry, Cambridge, UK, 2008).
- de Wijn, R. & van Gorkom, H.J. Kinetics of electron transfer from Q_A to Q_B in photosystem II. *Biochemistry* **40**, 11912–11922 (2001).
- Alonso-Mori, R. *et al.* Toward characterization of photo-excited electron transfer and catalysis in natural and artificial systems using XFELs. *Faraday Discuss.* **194**, 621–638 (2016).
- Messinger, J. *et al.* Absence of Mn-centered oxidation in the S₂ → S₃ transition: implications for the mechanism of photosynthetic water oxidation. *J. Am. Chem. Soc.* **123**, 7804–7820 (2001).
- Glatzel, P. & Bergmann, U. High-resolution 1s core hole X-ray spectroscopy in 3d transition metal complexes—electronic and structural information. *Coord. Chem. Rev.* **249**, 65–95 (2005).
- Yano, J. & Yachandra, V. Mn₄Ca cluster in photosynthesis: where and how water is oxidized to dioxygen. *Chem. Rev.* **114**, 4175–4205 (2014).
- Alonso-Mori, R. *et al.* A multicrystal wavelength-dispersive X-ray spectrometer. *Rev. Sci. Instrum.* **83**, 073114 (2012).
- Alonso-Mori, R. *et al.* Energy-dispersive X-ray emission spectroscopy using an X-ray free-electron laser in a shot-by-shot mode. *Proc. Natl. Acad. Sci. USA* **109**, 19103–19107 (2012).
- Alonso-Mori, R. *et al.* Photon-in photon-out hard X-ray spectroscopy at the Linac Coherent Light Source. *J. Synchrotron Radiat.* **22**, 612–620 (2015).
- Vankó, G. *et al.* Probing the 3d spin momentum with X-ray emission spectroscopy: the case of molecular-spin transitions. *J. Phys. Chem. B* **110**, 11647–11653 (2006).
- Svyazhin, A., Kurmaev, E., Shreder, E., Shamin, S. & Sahle, C.J. Local moments and electronic correlations in Fe-based Heusler alloys: K α X-ray emission spectra measurements. *J. Alloys Compd.* **679**, 268–276 (2016).
- Burgie, E.S. *et al.* Crystallographic and electron microscopic analyses of a bacterial phytochrome reveal local and global rearrangements during photoconversion. *J. Biol. Chem.* **289**, 24573–24587 (2014).
- Eldlund, P. *et al.* The room temperature crystal structure of a bacterial phytochrome determined by serial femtosecond crystallography. *Sci. Rep.* **6**, 35279 (2016).
- Bhattacharya, S., Auldrige, M.E., Lehtivuori, H., Ihalainen, J.A. & Forest, K.T. Origins of fluorescence in evolved bacteriophytochromes. *J. Biol. Chem.* **289**, 32144–32152 (2014).
- Zhang, C.F., Farrens, D.L., Bjorling, S.C., Song, P.S. & Kliger, D.S. Time-resolved absorption studies of native etiolated oat phytochrome. *J. Am. Chem. Soc.* **114**, 4569–4580 (1992).
- Mrogiński, M.A., Murgida, D.H. & Hildebrandt, P. The chromophore structural changes during the photocycle of phytochrome: a combined resonance Raman and quantum chemical approach. *Acc. Chem. Res.* **40**, 258–266 (2007).
- Braslavsky, S.E., Gärtner, W. & Schaffner, K. Phytochrome photoconversion. *Plant Cell Environ.* **20**, 700–706 (1997).
- Li, F. *et al.* X-ray radiation induces deprotonation of the bilin chromophore in crystalline *D. radiodurans* phytochrome. *J. Am. Chem. Soc.* **137**, 2792–2795 (2015).
- Lundin, D., Berggren, G., Logan, D.T. & Sjöberg, B.M. The origin and evolution of ribonucleotide reduction. *Life (Basel)* **5**, 604–636 (2015).

ONLINE METHODS

Samples. Photosystem II. PS II dimer was extracted and purified from *Thermosynechococcus elongatus* as reported previously⁴². PS II crystals ranging in size from 10 to 50 μm were then prepared by using an established seeding protocol⁴³. The crystals were transferred into a final buffer consisting of 0.1 M MES (pH 6.5), 0.1 M ammonium chloride, 10% (wt/vol) ethylene glycol and 35% (wt/vol) polyethylene glycol (PEG) 5000, with ~ 0.5 mM chlorophyll concentration, before loading into the sample delivery syringe (Hamilton gastight syringe, 500 μl).

The dimeric PS II samples were extracted and purified as described previously⁴⁴. The final chlorophyll concentration was adjusted to ~ 7.0 mM (70 mg/ml protein) in a final buffer comprising 0.1 M PIPES (pH 7.0), 5 mM calcium chloride, 30% (vol/vol) ethylene glycol and 0.02% (wt/vol) detergent β -dodecyl maltoside (βDM).

Phytochrome. *D. radiodurans* BphP apoproteins, bearing an N-terminal T7 tag (MASMTGGQQMGRGS) and a C-terminal hexahistidine tag, were expressed in *Escherichia coli* BL21(DE3) cells as the PSM (residues 1–501) or the PAS–GAF region (residues 1–321; including the Tyr307Ser-encoding mutation⁴⁵) using the pET21b plasmid (Novagen, Madison, WI). Cultures were grown at 16 °C in terrific broth and harvested by centrifugation 16 h after inducing apoprotein expression with isopropyl-D-1-thiogalactopyranoside. The cell pellets were frozen in liquid nitrogen and stored at -80 °C.

Frozen pellets were resuspended in lysis buffer (10% (wt/vol) glycerol, 20 mM HEPES–NaOH (pH 7.8), 500 mM NaCl, 0.05% Tween 20, 30 mM imidazole, 1 mM phenylmethanesulfonyl fluoride and 1 mM 2-mercaptoethanol), sonicated and clarified by centrifugation. DrBphP apoproteins were enriched from the lysates by nickel-nitrilotriacetic acid (Qiagen, Valencia, CA) chromatography, using the lysis buffer for washing and the lysis buffer with 300 mM imidazole for elution. The DrBphP-containing eluates were incubated overnight with a molar excess of biliverdin (BV) (Frontier Scientific, Logan, UT), and the free BV was removed by filtration through a G-25 Sephadex column (GE Healthcare) equilibrated in the ion-exchange buffer (10% (wt/vol) glycerol, 20 mM HEPES–NaOH (pH 7.8), 20 mM NaCl and 10 mM 2-mercaptoethanol). The chromoproteins were then purified by ion-exchange chromatography using a Q-Sepharose HP column (GE Healthcare) and a 20–1000 mM linear NaCl gradient for elution. The PAS–GAF chromoprotein was exchanged into 30 mM Trizma base–HCl (pH 8.0), and the PSM was exchanged into 10 mM HEPES–NaOH (pH 7.8) using a 50 ml G-25 Sephadex column (GE Healthcare), frozen as 30–50 μl droplets in liquid nitrogen and stored at -80 °C.

Crystallization of DrBphP chromoproteins was conducted in batch mode. PAS–GAF chromoproteins (at 40 mg/ml) were mixed at a 1:1 volumetric ratio with 15–16% (wt/vol) PEG3350, 19% (vol/vol) isopropanol, 5% (wt/vol) glycerol and 100 mM tetrasodium citrate–citric acid (pH 5.6). 2 ml batches were then seeded with 10 μl of a finely crushed PAS–GAF crystal slurry. PSM crystals were produced in the same manner, except that the crystallization solution contained 22–28% (wt/vol) PEG3350, 2.5% (vol/vol) Tacsimate (pH 6.0), 2.5% (vol/vol) Tacsimate (pH 7.0), 2% (vol/vol) ethylene glycol and 100 mM PIPES–NaOH (pH 6.5). Crystalline samples were mobilized by scraping with a pipet tip and suspended by aspiration. The crystal slurry was then loaded into a Hamilton syringe for sample delivery.

Ribonucleotide reductase. A crystallizable construct of the RNR R2 from *S. erythraea* was purified and prepared as described previously⁴⁶. Crystals suitable for the XFEL experiment were obtained at 20 °C under aerobic conditions using the batch crystallization method, in a 1:1 protein solution to crystallization buffer ratio. The crystallization buffer (10% (wt/vol) PEG3350 and 1% (vol/vol) Tacsimate (pH 4.0) was slowly released at the bottom of a tube containing a 20 mg/ml protein solution in a manner such that phase separation occurred between the upper protein solution and the lower crystallization buffer. The tube was incubated upright without mixing, for crystal growth. A pellet of up to 30 μm square-bipyramidal-shaped crystals appeared overnight. This crystal pellet was then resuspended in the crystallization buffer that was supplemented with 10% glycerol, and it was loaded into the sample delivery syringe used for data collection.

For solution XES measurements, a histidine-tagged construct encoding Ct R2 was expressed, and the protein was purified as previously described^{19,47}. The resulting apo-protein was anaerobically reconstituted with 0.75 equivalents of Fe(II) and Mn(II) per monomer. Representative images of crystals of all four samples used for the data collection are shown in **Supplementary Figure 3**.

Sample analysis with DOT. *Cleaning and drying the belt for continuous use.* During operation of the DOT setup, residual sample was removed continuously from the polyimide belt. After passing the X-ray probe point, the belt was immersed in a water tank, where four high-pressure water jets were used to remove sample debris. To remove waste and to maintain a constant level in the tank, water was drained using a peristaltic pump (Masterflex L/S digital pump, HV-77921-75, Cole-Parmer Instrument Company, LLC, USA). Water jets were produced through 250 μm inner-diameter PEEK tubing (part no. 1531, IDEX Health and Science LLC, USA) and generated by an HPLC pump (Prep 100 pump, P40PFT01, Scientific Systems, Inc., USA) at 100 ml/min, which produced an effective pressure of 800 psi. The belt was then dried with helium that was forced through small-diameter nozzles (Atto super air nozzle, model 1108SS, EXAIR Corporation, USA). To minimize helium consumption, the gas was continuously circulated using a compressor that comprised a diaphragm pump (KNF Neuberger, Inc., type N145.1.2AN.18) and a small reservoir. This mechanism was necessary to have enough backing pressure to purge water from the belt surface. Effective drying was also important for the operation of the rollers to maintain a constant tape speed and was achieved by blowing helium at a flow rate of 100 standard cubic feet (SCF)/h with a backing pressure of 20 psi.

Sample delivery system. The tape drive instrumentation included a 15 MHz spot-focused piezoelectric immersion transducer (part no. V319, Olympus NDT) with a focal length of 1.0 in. A waveform generator (model 33612A, Keysight Technologies) triggered by the XFEL master clock was used to produce short bursts of radio-frequency energy, which were amplified by a 500 W RF amplifier (model 500A250C, Amplifier Research, Souderton, PA, USA) and used to drive the transducer for droplet ejection. The transducer was immersed in degassed water within a three-dimensional (3D)-printed plastic sleeve with a sample reservoir at the end. A motorized stage was used to adjust the up-and-down position of the transducer such that the acoustic energy was focused at the liquid–gas interface. To change the position of the droplet deposition parallel to the beam, a second motorized stage

was used to move the transducer and sleeve together. The sample reservoir was a 3D-printed small plastic well (6 μl volume) with a thin polypropylene window to minimize the attenuation of the acoustic ejection pulse. Sample was continuously fed to the reservoir, using a syringe pump, through a 250 μm inner-diameter glass capillary. To avoid crystal settling, the syringe pump was mounted onto a shaker that rotated the syringe 180°. The 3D files and schematics of custom-built parts and more details of the sample delivery system are included in the **Supplementary Protocol**⁴⁸.

Laser excitation system. A Coherent Evolution frequency-doubled Nd:YLF laser provided 100 ns pulses of 527 nm light, which were fiber-coupled into the multi-flash excitation system depicted in **Supplementary Figure 1**. An identical and independent Evolution laser provided the free-space excitation pulse near the X-ray interaction region for studies of PS II. For all of the excitations in the PS II studies, a fluence of 0.12 J/cm² was used, with a focal diameter of 400 μm . The penetration depth of PS II at 527 nm is about 50 μm in PS II crystals and 400 μm in PS II solution at the concentrations we used. Thus, we are close to the limit in crystal size that can be excited from a single side. For solution samples, the situation was better, as the concentration was about 10 \times less.

Gas activation system. The oxygen incubation chamber (**Fig. 3a**) that was used for the solution studies of RNR was 3D printed using ABS-like resin, and it had five internal chambers. The central compartment, where O₂ gas is pumped, is a 60 mm long cylinder 14 mm in diameter. The flanking chambers, two on each side, are 15 mm long and 14 mm in diameter for each. To mount the conveyor belt on the drive, the top half of the chamber was made to be removable, and after mounting the belt, the chamber top was sealed to the bottom half with the aid of vacuum grease. Entrance holes into the sides of the O₂ activation chamber and between the internal chambers measured 0.9 mm in height by 3 mm in width. The vacuum pressure on the chambers immediately flanking the central O₂ chamber was set to −0.5 psig through a variable vacuum regulator. More details of the gas activation system are included in the **Supplementary Protocol**⁴⁸.

Data collection. The DOT setup was used at two end stations in Linac Coherent Light Source (LCLS): X-ray Pump Probe⁴⁹ (XPP) and Macromolecular Femtosecond Crystallography (MFX). Studies involving photoactivation began at XPP and continued at MFX over several beam times. Studies involving chemical activation were performed at MFX. The X-ray beam, with a pulse width of ~50 fs, was focused at either end station to 5 \times 5 μm^2 (FWHM) using beryllium lenses. A pulse energy of 2.5 mJ at 9.5 keV, corresponding to $\sim 1.6 \times 10^{12}$ photons/pulse, was used at a repetition rate of 10 Hz for crystal samples. For XES, solution samples of PS II were excited at 7.5 keV and at 30 Hz repetition rate. Fe XES of the RNR solution was collected at 60 Hz using 9.5 keV excitation and 2.5 mJ pulse energy. To minimize the belt diffraction background, the tails of the beam were obscured with a pinhole lead collimator. XRD data were collected in the forward direction with a Rayonix MX 170 HS detector at a distance of 58 to 108 mm from the interaction point, allowing for detection of a maximum inscribed resolution of 1.4 or 2.0 Å, respectively. To calibrate the detector distance, the XRD pattern of silver behenate, enclosed in a quartz capillary (Hampton Research, 10 μm wall thickness,) was recorded with an attenuated beam

($\leq 1\%$). Mn XES spectra were recorded perpendicular to the beam on a Cornell-SLAC pixel-array detector (CSPAD-140k)⁵⁰ using a multicrystal wavelength-dispersive hard X-ray spectrometer based on the von Hamos geometry²⁹. Studies on Fe K α XES used the newly available ePIX-100 detector⁵¹ in the same geometry. Mn XES was analyzed by an array of 16 silicon crystal analyzers (using the 440 reflection plane; hereafter referred to as '(440)') that were mounted at a distance of 500 mm from the interaction point, with the center of the array at an angle of 81° with respect to the interaction point. The Bragg angle range covered by these analyzer crystals was 85.8–83.4°, which corresponds to a Mn K $\beta_{1,3}$ energy range from 6,474.6 to 6,499.4 eV. To calibrate the emission energy, the XES spectrum of the MnCl₂ solution (500 mM), in a quartz capillary, was collected by using an unfocused beam. The emission energy was then calibrated to the published value of 6,493.3 eV of MnCl₂ spectrum peak position³⁰. Fe K α XES was analyzed by a single germanium (440) crystal placed 250 mm from the interaction point, with the center of the crystal at an angle of 75.41° with respect to the interaction point, and resolved both K α lines from 6,370 to 6,420 eV. Calibration of the Fe spectrometer was similar to the method used for Mn, using as the reference Fe(III)(NO₃)₃ instead.

Data processing. *Processing of data of raw XRD images.* Analysis of the diffraction data was performed using cctbx.xfel^{52,53}. Diffraction images were indexed using LABELIT⁵⁴ with a target cell to guide the choice of basis vectors. For PS II samples, two populations of unit cells in the $P2_12_12_1$ space group were identified (isoform A: $a = 117.5$ Å, $b = 223.6$ Å, $c = 329.5$ Å; isoform B: $a = 117.7$ Å, $b = 223.2$ Å, $c = 310.5$ Å). PS II diffraction images were re-indexed twice, imposing either isoform A or isoform B unit cell parameters as constraints during unit cell refinement, to generate two disjoint sub-data sets for each illuminated state. For other samples, the single predominant unit cell identified in the first indexing step was imposed as a basis set target and a unit cell constraint in a second round of indexing. For all samples, resolution limits were determined independently for each image to ensure that the weak signal at high resolution in the highest-resolution images was not diluted by noise contributions from lower-resolution images. To determine resolution limits on each image, reflections were sorted into bins of equal size by resolution, and all bins beyond and including the lowest-resolution bin in which the average signal to uncertainty ratio ($I/\sigma(I)$) was below 0.1 were discarded. This approach permits the inclusion of a small number of negative intensities, while in practice eliminating most nonphysical negative-intensity reflections. Signal was integrated to these resolution limits, and the resulting data were merged using the program cxi.merge. The resolution cut-off for the final merged data was determined based on a combination of several criteria, including where the data fell below 10-fold multiplicity, where the $CC_{1/2}$ became 'unstable' (meaning it began to oscillate at higher resolution instead of uniformly decreasing) and where the values of $I/\sigma(I)$ did not uniformly decrease any more.

Roughly half of the forward scattering signal passes through the polyimide belt, slightly lowering the Bragg spot intensities in this region. We developed a ray-tracing model to predict the absorption by the belt at a given point on the detector and used this to correct Bragg intensities during integration. Our model uses three fit parameters: distance of the crystal from the edge of the belt f ,

crystal height h , and the angle Θ between the vertical axis of the detector and the conveyor belt. Belt thickness and material absorption cross-section are treated as known constants. These various parameters are illustrated in **Supplementary Figure 2c**, with the overall problem depicted in **Supplementary Figure 2b**. Parameters f , h and Θ were obtained indirectly through geometric relations to two boundary lines that were observed on the detector. The boundary lines (corresponding to maximum and minimum belt absorption) are highlighted in **Supplementary Figure 2a,c** in red and blue, respectively. An estimate for the uncertainty of the Bragg spot intensity is needed in subsequent processing steps to weight observations. The uncertainty of the absorption correction to the spot intensity was estimated by the change in spot intensity after perturbing the fit parameters. We typically found that the perturbations in f produced the largest effect and that perturbations on the order of a droplet diameter dominated other uncertainty estimates. Consequently, Bragg spots, which are shadowed by the belt, were down-weighted relative to those that were unshadowed during merging. Separate resolution cut-offs were used for Bragg spots that were affected and unaffected by Kapton-belt absorption.

XES data reduction and analysis. **Supplementary Figure 7a** shows the raw data of the averaged XES spectrum collected with the pixel-array detector. To subtract the background signal, a fifth-order two-dimensional polynomial background was fit to the image using information outside of the region of interest (ROI), shown bounded by red lines. The fit of the background was extrapolated into the ROI (**Supplementary Fig. 7b**; with the intensity multiplied by 4) to estimate its intensity there. The estimated background is shown as the red line in **Supplementary Figure 7c**. The final XES spectrum was obtained by integrating a tight ROI around the background-subtracted signal (depicted in **Supplementary Fig. 7d**). The resulting spectrum is shown in **Supplementary Figure 7e**. Difference spectra were computed by normalizing the component spectra by their respective sums and then subtracting the components.

Synchrotron XES data collection. Room temperature Mn $K\beta_{1,3}$ XES difference spectra in **Figure 2** are shown with reference to the corresponding cryogenic difference spectra of PS II S states collected at BL 6-2 of the Stanford Synchrotron Radiation Light source (SSRL). For these synchrotron measurements, the incidence energy was set to 10.4 keV with the beam line monochromator, which uses two cryogenically cooled silicon crystals in '111' reflection. The X-ray beam was focused to 0.45 mm (vertical) \times 0.45 mm (horizontal) (FWHM) by means of vertical and horizontal focusing mirrors. The X-ray flux at 10.4 keV was $\sim 1 \times 10^{13}$ photons/s/mm². Samples were prepared in 0, 2 and 3 flash states by a freeze-quench method, in which a sample holder containing a 300 μ m thick layer of PS II solution from *T. elongatus* (8.5 mM chlorophyll) was flashed from two sides with a Spectra-Physics Quanta Ray Pro 230-10 Nd:YAG laser (0.3 J/cm², 9 ns pulse duration) with a 1 s flashing interval and subsequently plunged (within 1 s) into liquid nitrogen. During the measurement, samples were kept at a temperature of 10 K in a continuous-flow liquid helium cryostat (Oxford Instruments CF1208) under a helium-exchange gas atmosphere. Emission spectra were recorded by means of a high-resolution crystal-array spectrometer, using the 440 reflection of seven spherically bent Si(110) crystals (100 mm diameter, 1 m radius of curvature), aligned on intersecting Rowland circles. An energy-resolving Si drift detector (Vortex) was positioned at

the focus of the seven diffracting elements. A helium-filled polyethylene bag was placed between the cryostat and the spectrometer to minimize signal attenuation due to air absorption. Each energy point in the spectra was collected at a fresh sample spot. The maximum exposure time at each spot was 2.5 s, and the signal was read out in bins of 50 ms duration. To determine an appropriate exposure time to avoid radiation-induced effects, the signal intensity was measured as a function of exposure time at a single emission energy for each S state. No significant changes were observed within the first 1.5 s of exposure, and so 20 time bins (equivalent to 1 s) were averaged for the final spectra. The signal intensity from each sample spot was normalized by the emission signal intensity recorded at 6,491.5 eV within 7 s from the same sample spot, after going through all the fresh spots.

Structure determination. Phytochrome structural determination, model building and refinement. Initial phases for the PAS-GAF and PSM data sets were calculated by PHASER⁵⁵ (using the 1.45 Å DrBphP PAS-GAF structure (PDB ID code 2O9C) generated by Wagner *et al.*⁴⁵ as the search model for the PAS and GAF domains, and residues 325–501 of PDB ID 4Q0J as the PHY domain search model for the PSM³⁴). To minimize model bias at the chromophore, the biliverdin and side chains of the following residues were omitted during molecular replacement and initial structural refinements: Cys24, Ile29, Arg70, Met174, Tyr176, Glu193, His196, Phe198, Phe203, Asp207, Ile208, Pro209, Tyr216, Arg222, Arg254, Ser257, Met259, His260, Tyr263, Leu264, Met267, Ser272, Ser274, Leu286, His290 and Arg310. Manual model building was conducted with COOT⁵⁶, and structures were refined and simulated-annealing omit maps were calculated with PHENIX⁵⁷. The initial refinement for each structural model included simulated annealing to reduce model bias. Model validation was conducted with MOLPROBITY⁵⁸, and superpositions and figure preparation were conducted with the PyMOL Molecular Graphics System.

RNR structure determination, model building and refinement. The RNR structure was solved using PHASER⁵⁵ by molecular replacement using the atomic coordinates of the R2 subunit of ribonucleotide reductase from *C. trachomatis* (PDB ID 1SYU)⁵⁹ as a starting model. A well-contrasted solution was obtained with 1 molecule per asymmetric unit (space group $P4_12_12$). A preliminary crystallographic refinement was performed using PHENIX⁵⁷, and the 3D model was examined and modified using the program COOT⁵⁶. **Supplementary Table 2** lists the crystallographic statistics in which the test set represents 5% of the reflections. The current Ramachandran plot indicates that 93.0% and 0.3% of the residues are in the favored and disallowed regions, respectively. **Figure 4e** was prepared using the PyMOL Molecular Graphics System.

Data availability. Accession codes. Coordinates and structure factors of the phytochrome PAS-GAF and PSM structures have been deposited in the RCSB Protein Data Bank under accession codes 5MG0 and 5MG1, respectively. Source data files for **Figure 2–4** and **Supplementary Figures 4** and **7** are available online.

Code availability. Source code for the cctbx.xfel software package, which was used for diffraction data processing, is freely available and is distributed via the PHENIX software package (<http://phenix-online.org/>). Further information can be obtained via the cctbx.xfel homepage (<http://cci.lbl.gov/xfel/>).

42. Hellmich, J. *et al.* Native-like photosystem II superstructure at 2.44 Å resolution through detergent extraction from the protein crystal. *Structure* **22**, 1607–1615 (2014).
43. Ibrahim, M. *et al.* Improvements in serial femtosecond crystallography of photosystem II by optimizing crystal uniformity using microseeding procedures. *Struct. Dyn.* **2**, 041705 (2015).
44. Kern, J. *et al.* Purification, characterization and crystallization of photosystem II from *Thermosynechococcus elongatus* cultivated in a new type of photobioreactor. *Biochim. Biophys. Acta* **1706**, 147–157 (2005).
45. Wagner, J.R., Zhang, J., Brunzelle, J.S., Vierstra, R.D. & Forest, K.T. High-resolution structure of *Deinococcus* bacteriophytochrome yields new insights into phytochrome architecture and evolution. *J. Biol. Chem.* **282**, 12298–12309 (2007).
46. Kutin, Y. *et al.* Divergent assembly mechanisms of the manganese-iron cofactors in R2lox and R2c proteins. *J. Inorg. Biochem.* **162**, 164–177 (2016).
47. Dassama, L.M.K. *et al.* O₂-evolving chlorite dismutase as a tool for studying O₂-utilizing enzymes. *Biochemistry* **51**, 1607–1616 (2012).
48. Fuller, F.D. *et al.* Droplet on tape: protocol. *Nat. Protoc.* <http://dx.doi.org/10.1038/protex.2017.017> (2017).
49. Chollet, M. *et al.* The X-ray pump-probe instrument at the Linac coherent light source. *J. Synchrotron Radiat.* **22**, 503–507 (2015).
50. Herrmann, S. *et al.* CSPAD-140k: a versatile detector for LCLS experiments. *Nucl. Instrum. Methods Phys. Res. A* **718**, 550–553 (2013).
51. Carini, G. *et al.* in 2014 IEEE Nuclear Science Symposium and Medical Imaging Conference (NSS/MIC) 1–3 (IEEE, Seattle, WA, USA; 2014).
52. Sauter, N.K., Hattne, J., Grosse-Kunstleve, R.W. & Echols, N. New Python-based methods for data processing. *Acta Crystallogr. D Biol. Crystallogr.* **69**, 1274–1282 (2013).
53. Hattne, J. *et al.* Accurate macromolecular structures using minimal measurements from X-ray free-electron lasers. *Nat. Methods* **11**, 545–548 (2014).
54. Sauter, N.K., Grosse-Kunstleve, R.W. & Adams, P.D. Robust indexing for automatic data collection. *J. Appl. Crystallogr.* **37**, 399–409 (2004).
55. McCoy, A.J. *et al.* Phaser crystallographic software. *J. Appl. Crystallogr.* **40**, 658–674 (2007).
56. Emsley, P. & Cowtan, K. Coot: model-building tools for molecular graphics. *Acta Crystallogr. D Biol. Crystallogr.* **60**, 2126–2132 (2004).
57. Adams, P.D. *et al.* PHENIX: a comprehensive Python-based system for macromolecular structure solution. *Acta Crystallogr. D Biol. Crystallogr.* **66**, 213–221 (2010).
58. Chen, V.B. *et al.* MolProbity: all-atom structure validation for macromolecular crystallography. *Acta Crystallogr. D Biol. Crystallogr.* **66**, 12–21 (2010).
59. Högbom, M. *et al.* The radical site in chlamydial ribonucleotide reductase defines a new R2 subclass. *Science* **305**, 245–248 (2004).